Journal of Power Sources 248 (2014) 647–654

Contents lists available at ScienceDirect

Journal of Power Sources

journal homepage: www.elsevier.com/locate/jpowsour

An investigation on strontium doped $Sm_2NiO_{4+\delta}$ cathode for intermediate temperature solid oxide fuel cells

V.N. Chaudhari [1], A.P. Khandale [1], S.S. Bhoga*

Department of Physics, Rashtrasant Tukadoji Maharaj Nagpur University, Nagpur 440 033, India

HIGHLIGHTS

- $Sm_{2-x}Sr_xNiO_{4+\delta}$ ($x = 0.4–1.0$) solid solutions crystallites are of 73–82 nm.
- Orthorhombic phase forms when $x = 0.4–0.7$ and tetragonal when $x = 0.8–1.0$.
- Narrow particle size distribution with effective size 423.44 ± 11.87 nm in ink.
- Minimum ASR = 2.7 Ω cm^2 at 700 °C obtained when $x = 0.5$.
- Lowest ASR is attributed to uniform sub-micron grains.

ARTICLE INFO

Article history:
Received 21 August 2013
Received in revised form
23 September 2013
Accepted 26 September 2013
Available online 11 October 2013

Keywords:
Mixed ionic–electronic conductor
Cathode
Area specific resistance
Electrochemical impedance spectroscopy
Symmetric cell
Particle size distribution

ABSTRACT

The $Sm_{2-x}Sr_xNiO_{4+\delta}$ when $x = 0.4–1.0$ solid solutions are synthesized by combustion followed by sintering at 1100 °C for 10 h, yield crystallite size in the range 73–82 nm. The single-phase $Sm_{2-x}Sr_xNiO_{4+\delta}$ are of orthorhombic and tetragonal crystal structures when $x = 0.4–0.7$ and $x = 0.8–1.0$, respectively. The maximum electronic conductivity ($\sigma = 0.361$ S cm^{-1} at 640 °C) for $Sm_{1.5}Sr_{0.5}NiO_{4+\delta}$ is due to the extrinsic defects. The decrease in conductivity when $x > 0.5$ is attributed to the formation of electrically neutral clusters. The narrow particle size distribution with mean particle size 423 ± 11 nm, of $Sm_{1.5}Sr_{0.5}NiO_{4+\delta}$ is obtained by ball milling the ink/slurry at 300 revolutions per minute (rpm) for 1 h. The minimum area specific resistance (ASR) of 2.7 Ω cm^2 at 700 °C is obtained when $x = 0.5$, and is attributed to uniform superfine grains and optimum porosity of cathode.

1. Introduction

In the recent past, the mixed ionic–electronic conductors (MIECs) have been considered as a potential cathode for intermediate temperature solid oxide fuel cells (IT-SOFCs) due to high oxygen tracer diffusion coefficients and good electronic conductivity [1–4]. Rare-earth nickelates with K_2NiF_4-type structure, general formula $Ln_2NiO_{4+\delta}$ (Ln = La, Pr, Nd), have shown promising performance as cathode with various electrolyte materials, such as yttria stabilized zirconia (YSZ), samarium doped ceria (SDC) and $La_{1-x}Sr_xGa_{1-y}Mg_yO_{3-\delta}$ (LSGM) [5–8]. The K_2NiF_4-type structure consists of perovskite layer of $LnNiO_3$ separated by rocksalt layer of LnO, with a network of unoccupied interstitial sites. Upon oxidation of the material, excess oxygen can be accommodated in the interstitial sites and compensate for the formation of Ni holes in the form of Ni^{3+} [9,10]. The thermo-chemical stability of K_2NiF_4-type manganates, ferrates, cuprates and nickelates exhibited higher values than those of the corresponding perovskite-type oxides [11]. Sr-doping in La_2NiO_4 reported to improve p-type electrical conductivity (30–60 S cm^{-1}) [12]. According to literature, different kinds of defects can be formed in K_2NiF_4-type structure depending on Sr-doping, oxygen partial pressure and preparation temperature [13–15]. Li et al. [16] have reported minimum ASR (3.06 Ω cm^2 at 700 °C) for $Sm_{1.0}Sr_{1.0}NiO_{4\pm\delta}$ prepared by glycine–nitrate process.

A close scrutiny of the literature revealed that the $Sm_{2-x}Sr_xNiO_{4+\delta}$ is less attempted as cathode for IT-SOFCs application. Moreover, there is enough scope for preparing superfine polycrystalline $Sm_{2-x}Sr_xNiO_{4+\delta}$ through alternative routes to improve upon their electrical and electrochemical properties. The

* Corresponding author. Tel.: +91 9822366066; fax: +91 7122500736.
E-mail address: msrl.physics1@gmail.com (S.S. Bhoga).
[1] Tel.: +91 9822366066; fax: +91 7122500736.

0378-7753/$ – see front matter © 2013 Elsevier B.V. All rights reserved.
http://dx.doi.org/10.1016/j.jpowsour.2013.09.115

present study was aimed at preparation of $Sm_{2-x}Sr_xNiO_{4+\delta}$ ($x = 0.0$–1.0) solid solutions using combustion (without fuel) synthesis. The samples were characterized using X-ray powder diffraction, scanning electron microscopy, particle size distribution and four-probe dc conductivity. Additionally, electrochemical impedance spectroscopy (EIS) studies on the symmetric cells with Cathode/GDC/Cathode configuration were carried out as a function of temperature and oxygen partial pressure.

2. Experimental

The $Sm_{2-x}Sr_xNiO_{4+\delta}$ (0.0–1.0) powders were prepared using combustion technique [17]. Initial reagents samarium acetate, strontium acetate and nickel acetate (Aldrich Chemicals, USA) were of purity > 99.9%. All the above-mentioned reagents were dried at 120 °C for 6 h in order to remove the traces of moisture present. Each of the respective requisite reagents in their stoichiometric ratio was dissolved in the double distilled deionized water, separately. All the solutions were mixed together in a single corning flask. Later, the homogeneous aqueous solution was heated at 100 °C while subjecting it to a constant stirring using rota-mantle till evaporation of the water. The precipitate, thus obtained, was then charred at about 250 °C by introducing it in an electric muffle furnace. Pellets of diameter 9 mm and thickness 2 mm were obtained by uniaxially compressing ground powder at 2.94 N m^{-2} pressure with the help of Specac (UK) stainless steel die-punch and hydraulic press. The resulting pellets were finally sintered at 1100 °C for 10 h. The $Sm_{2-x}Sr_xNiO_{4+\delta}$ when $x = 0.4$, 0.5, 0.6, 0.8, and 1.0 are hereafter designated as SSNO-0.4, SSNO-0.5, SSNO-0.6, SSNO-0.8, and SSNO-1.0, respectively.

The thin platinum film on both the flat surfaces of sintered pellet was obtained by dc sputtering resulting in good ohmic contacts for d.c. electrical conductivity measurements. Four wire measurements eliminate the lead wire resistance. A schematic presentation of set up for temperature dependent d.c. conductivity measurements and sample holder are shown in Fig. 1(a) and (b), respectively. Prior to the conductivity measurement the sample (sintered pellet), spring-loaded in a ceramic cell holder (Fig. 1(b), Amel, Italy), was heated to 700 °C for 1 h so as to homogenize the charge carriers. The resistance as a function of temperature, during the cooling cycle, was measured using four-probe method with the help of computer controlled Keithley 6221 current source and 2182A nanovoltmeter in delta mode. The temperature of the sample during measurement was controlled with an accuracy of ±1 °C with the help of Eurotherm 2216e temperature controller. The predetermined oxygen partial pressure (0.1–21%) around the cell during the conductivity measurements was maintained using electronic mass flow meters cum controllers, Teledyne-Hastings, USA. Nitrogen was used as carrier gas. The gas flow rate was 200 SCCM during the measurements.

The ink/slurry of optimized cathode $Sm_{1.5}Sr_{0.5}NiO_{4+\delta}$ (on the basis of dc conductivity) was obtained as follows. 1 g of $Sm_{2-x}Sr_xNiO_{4+\delta}$ powder was mixed with 3 wt% polyvinyl buteral (binder), sodium free corn oil and ethyl methyl ketone. The mixture was then ball milled with 300 revolutions per minute (rpm) for 1 h with the help of planetary monomill, Fritsch Pulverisette-6, Germany. The 35 tungsten carbide balls of 10 mm diameter and 80 ml bowl of same material were used. The GDC (10 mol% gadolinium doped ceria) nano-powder (Aldrich, USA) was pressed as described above to obtain pellets of 9 mm diameter and 1 mm thickness. Later, they were sintered at 1400 °C for 6 h. The sintered density of 96% was achieved. Both the flat surfaces of the GDC pellet were then roughened with # 60 grit paper and cleaned with acetone. The slurry/ink of cathode material was then spin coated with a spin coater at 3000 rpm for 60 s on each of the flat surfaces of sintered

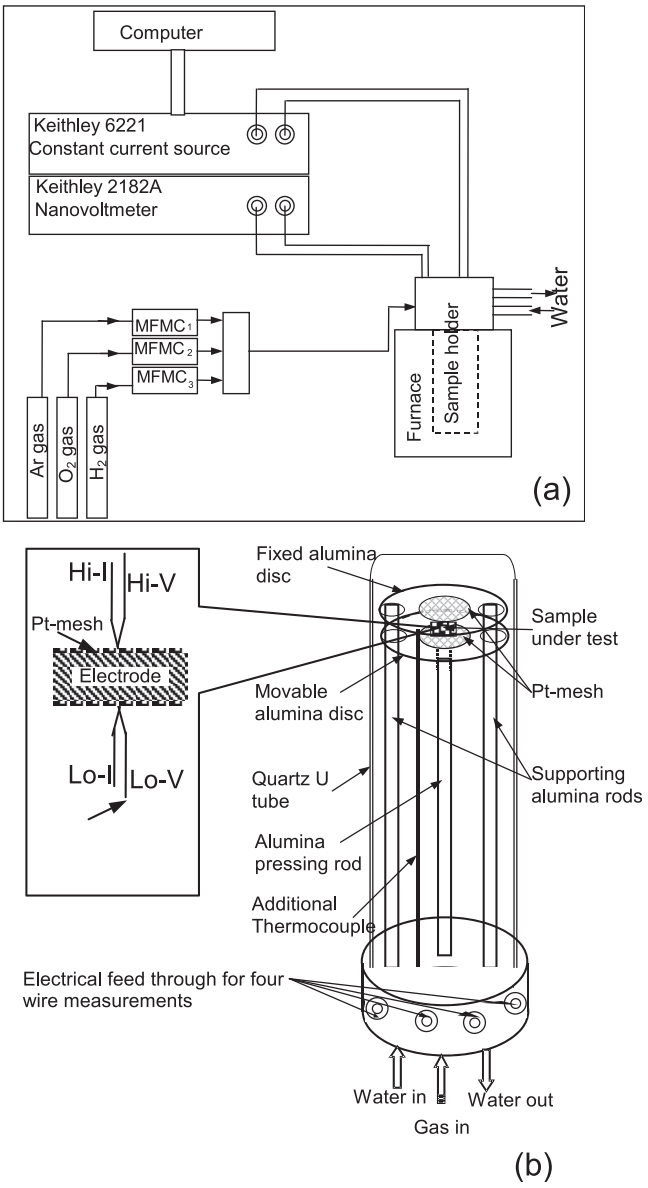

Fig. 1. A schematic presentation of (a) set up for temperature dependent d.c. conductivity measurement and (b) sample holder; inset shows the configuration of four wire contact with sample (Hi-V, Lo-V, Hi-I and Lo-I are high voltage, low voltage, high current and low current terminals, respectively).

GDC electrolyte to obtain symmetric cells, $Sm_{1.5}Sr_{0.5}NiO_{4+\delta}$/GDC/$Sm_{1.5}Sr_{0.5}NiO_{4+\delta}$. The cells sintered at 800, 900, and 1000 °C are designated as Cell-8, Cell-9, and Cell-10, respectively.

All the sintered samples were characterized using X-ray powder diffraction (XRD), PANalytical X'pert PRO (Philips, The Netherlands) using CuK_α radiations. The curved graphite crystal was used as a monochromator. The XRD measurements were carried out in the 2θ range from 10 to 100° with step size and time per step as 0.025° and 1 s, respectively. The crystallite size of all compositions under study was determined using X'pert High Score Plus software based on the Scherrer formula as described earlier [18]. The microstructure and elemental composition of the cathode of symmetric cells were examined using field emission scanning electron microscope (FESEM) with EDS, Jeol JSM 7600-F (Germany). The particle size distribution of cathode material in the ink/slurry was estimated using particle size analyzer, NanoPhox (Symphatec, Germany). The sintered densities of all the samples were determined using

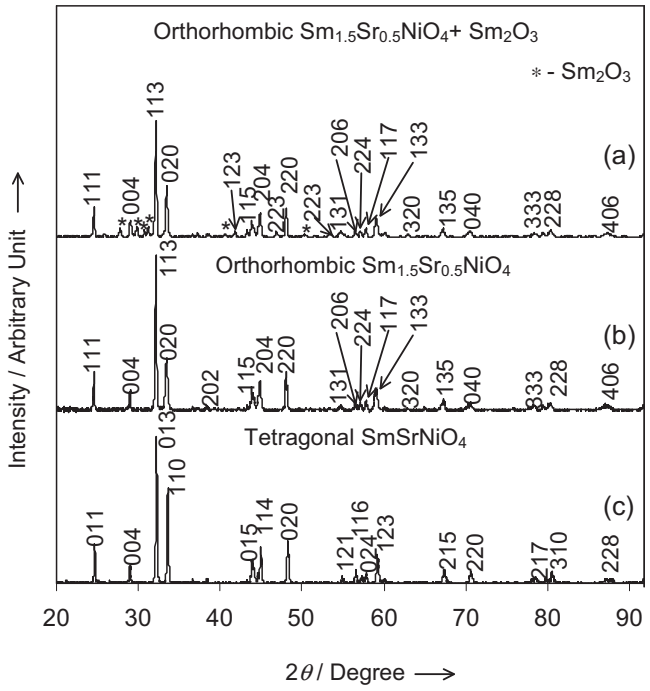

Fig. 2. The X-ray powder diffraction patterns of $Sm_{2-x}Sr_xNiO_{4+\delta}$ when (a) $x = 0.3$, (b) $x = 0.4$, and (c) $x = 0.8$.

Archimedes' principle using Metller Toledo monopan balance with density kit. Microhardness numbers, of all the samples under study, were measured by the Vickers indentation technique (HMV-2 microhardness tester, Shimadzu, Japan). The dc conductivity as a parametric function of temperatures was measured on sintered pellets in the temperature range 500–700 °C using four-probe method [18].

EIS measurements on the symmetric cells were carried out using a computer-controlled Solartron 1255B FRA in combination with a Solartron SI 1287 electrochemical interface as a function of temperature, frequency range 1×10^{-3}–1×10^{6} Hz, and oxygen partial pressure (0.1–21%) as described elsewhere [18]. The applied ac signal voltage was 50 mV.

3. Results and discussion

3.1. X-ray powder diffraction and energy dispersive x-ray spectroscopy

Typical X-ray powder diffraction (XRD) patterns of $Sm_{2-x}Sr_xNiO_{4+\delta}$ when $x = 0.3$, 0.4 and 0.8 are shown in Fig. 2(a)–(c), respectively. In general, all the diffracted lines are broader than usually observed for good crystalline solids. The broadening of diffracted lines is, thus, attributed to the superfine crystalline nature of materials. Before indexing, the obtained XRD data were subjected to profile fitting with the help of X'pert High Score Plus software. A close look at the Fig. 2(a) reveals the presence of diffracted peaks due to $Sm_{1.5}Sr_{0.5}NiO_{4+\delta}$ (joint committee for powder diffraction standards, JCPDS, file No.00-045-0247) and Sm_2O_3 (JCPDS file No.00-042-1464). Similar results were observed for $Sm_{2-x}Sr_xNiO_{4+\delta}$ when $x = 0.1$–0.2 indicating non-formation of solid solution up to $x = 0.3$ in spite of sintering combusted powder (stoichiometric reagents) at 1100 °C for 10 h. On the other hand, all the experimental characteristics diffraction peaks ($x = 0.4$) closely match (Fig. 2(b)) with JCPDS data (file No.00-045-0247) corresponding to the orthorhombic $Sm_{1.5}Sr_{0.5}NiO_{4+\delta}$. Similar results were obtained when $x = 0.5$–0.7. All the experimental characteristic peaks of Fig. 2(c) (when $x = 0.8$) closely match with JCPDS data (file No.00-048-0973) due to tetragonal $SmSrNiO_{4+\delta}$. Absence of line(s) due to initial reagent when $x = 0.4$–1.0 confirms the formation of single-phase solid solutions. It can, thus, be concluded that $Sm_{2-x}Sr_xNiO_{4+\delta}$ when $x = 0.4$–0.7 and $x = 0.8$–1.0 are of orthorhombic and tetragonal crystal structures, respectively. These results are in good agreement with the reported data [19]. The materials with K_2NiF_4-type structure are stable only when the tolerance factor, t, is in the range $0.85 < t < 1.02$ [20]. The calculated values of t (based upon Shannon's ionic radii [21]) for $Sm_{2-x}Sr_xNiO_{4+\delta}$ when $x = 0.4$–1.0 are within the limits. Thus, the solid solutions form with K_2NiF_4-type structure when $x = 0.4$–1.0.

The experimental lattice cell constants determined from XRD data are compared in Table 1. As seen, the values of a, b and c when $x = 0.4$ are in close agreement with the report ($a = 0.53103$, $b = 0.53534$ and $c = 1.23415$ nm) for orthorhombic $Sm_{1.5}Sr_{0.5}NiO_{4+\delta}$ [19]. Similarly, the values of lattice cell constants a and c for $x = 0.8$ are in close agreement with the report ($a = 0.37859$ and $c = 1.22212$ nm) for tetragonal $SmSrNiO_{4+\delta}$ [19]. A close scrutiny of Table 1 reveals that, within the orthorhombic phase ($x = 0.4$–0.7), the lattice cell constant a remains almost unchanged, whereas the values of b and c change with x. The value of lattice cell constant c, however, increases appreciably with increase in Sr content. The value of lattice cell constant a varies negligibly in case of tetragonal solid solutions ($x = 0.8$–1.0). The value of c, however, increases proportionally with x. In general, a negligible change in the value of a, while increase/decrease in c with dopant concentration for the materials with K_2NiF_4-type structure is reported in literature [17,19]. The partial substitution of relatively bigger Sr^{2+} ($r^{2+}_{Sr} = 0.131$ nm) for Sm^{3+} ($r^{3+}_{Sm} = 0.1132$ nm) [21] (in coordination number, CN = 9) in both the orthorhombic and the tetragonal symmetry causes considerable increase in lattice cell constant c. Systematic variations of c and v in both the phases of $Sm_{2-x}Sr_xNiO_{4+\delta}$ (Table 1) suggest the formation of solid solutions without two-phase regions.

All the compositions under study show almost similar crystallite size (73–82 nm), sintered density (83–94%) and microhardness number (471–549 HV) values, as shown in Table 1. Evidently, there is no influence of dopant on microstructures of solid solutions. The experimental (as obtained from EDS) and theoretical values of at%

Table 1
A comparison of tolerance factor (t), crystal structure, lattice cell constants (a, b, c and v), average crystallite size (C_s), % density (ρ) and microhardness number (HV) of $Sm_{2-x}Sr_xNiO_{4+\delta}$ ($x = 0.4$–1.0).

x	t	Structure	a (nm)	b (nm)	c (nm)	v (nm^3)	C_s (nm)	ρ (%)	HV
0.4	0.926	Orthorhombic	0.532 ± 0.001	0.536 ± 0.0007	1.232 ± 0.0015	0.351 ± 0.063	77 ± 0.64	90.8 ± 0.1	471 ± 4
0.5	0.929	Orthorhombic	0.532 ± 0.0008	0.537 ± 0.0007	1.234 ± 0.0016	0.352 ± 0.067	73 ± 0.36	89.3 ± 0.4	501 ± 3
0.6	0.933	Orthorhombic	0.531 ± 0.0011	0.538 ± 0.0004	1.237 ± 0.0017	0.353 ± 0.062	82 ± 0.26	91.5 ± 0.3	496 ± 5
0.7	0.936	Orthorhombic	0.532 ± 0.0008	0.540 ± 0.0004	1.239 ± 0.0016	0.356 ± 0.063	79 ± 0.47	90.7 ± 0.4	536 ± 4
0.8	0.939	Tetragonal	0.377 ± 0.0001	0.377 ± 0.0001	1.231 ± 0.0005	0.175 ± 0.012	80 ± 0.64	94.9 ± 0.2	525 ± 6
0.9	0.942	Tetragonal	0.377 ± 0005	0.377 ± 0008	1.235 ± 0.0016	0.176 ± 0.063	78 ± 0.16	94.9 ± 0.4	519 ± 7
1.0	0.946	Tetragonal	0.377 ± 0.0003	0.377 ± 0.0003	1.237 ± 0.0016	0.177 ± 0.025	76 ± 0.37	89.4 ± 0.1	549 ± 4

Table 2
A comparison of experimentally and theoretically estimated at% values for elements of $Sm_{1.5}Sr_{0.5}NiO_{4+\delta}$.

Element	Concentration (at%)	
	Theoretical	Experimental
O	57.1428	57.86 ± 1.0
Ni	14.2857	13.75 ± 0.5
Sr	07.1429	07.137 ± 0.7
Sm	21.4286	21.316 ± 0.4
Total	100.000	100.00 ± 0.4

of elements of $Sm_{1.5}Sr_{0.5}NiO_{4+\delta}$ given in Table 2 are closely matching, which suggests formation of stoichiometric compound.

3.2. Scanning electron microscopy and particle size analysis

The scanning electron microphotographs (SEM) of the electrode surfaces of Cell-8, Cell-9, Cell-10, and fractured surface across the electrode–electrolyte interface of Cell-10 are depicted in Fig. 3(a)–(d), respectively. A close scrutiny of Fig. 3(a)–(c) reveals agglomerated lumps of sub-micron size grains of $Sm_{1.5}Sr_{0.5}NiO_{4+\delta}$ with uniformly distributed micro-pores throughout the cathode. Further, electrode and electrolyte form homogenous contacts along the interface (Fig. 3(d)). In spite of heating and cooling cycles over four runs, no cracks or separation between the electrode and the electrolyte are observed. It can, also, be inferred from Fig. 3(d) that the electrode structure is highly porous with an average thickness of 23.5 ± 1.6 μm, and GDC electrolyte is almost fully dense.

The particle size distribution of $Sm_{1.5}Sr_{0.5}NiO_{4+\delta}$ in the prepared ink (five batches) is shown in Fig. 4. As seen, the particle sizes and their distribution are almost same indicating reproducible results. The effective particle size is 423 ± 11 nm. The particle size distribution is narrow.

3.3. d.c. Conductivity

The variation of d.c. conductivity as a parametric function of temperature for $Sm_{2-x}Sr_xNiO_{4+\delta}$ when $x = 0.4$, 0.5, 0.6, 0.8 and 1.0 is shown in Fig. 5. All the samples, within the temperature range of measurements, obey the Arrhenius law,

$$\sigma T = (\sigma T)_0 \exp\left(\frac{-E_a}{kT}\right), \quad (1)$$

where $(\sigma T)_0$, k, T and E_a are pre-exponential factor, Boltzmann constant, absolute temperature and activation energy, respectively. The conductivity initially increases with increase in Sr content in $Sm_{2-x}Sr_xNiO_{4+\delta}$. After attaining a maximum in conductivity when $x = 0.5$ it decreases (inset of Fig. 5). The activation energy determined for SSNO-0.4, SSNO-0.5, SSNO-0.6, SSNO-0.8, and SSNO-1.0 are 0.27, 0.26, 0.32, 0.33, and 0.36 eV, respectively. Evidently, the composition exhibiting minimum activation energy coincides with the composition that has maximum conductivity.

The conductivity behavior is Sr concentration dependent (inset of Fig. 5) and can be understood on the basis of defect chemistry. The most probable defects in $Sm_{2-x}Sr_xNiO_{4+\delta}$ are Sr^{2+} at Sm^{3+} regular lattice site with one negative charge (Sr'_{Sm}), interstitial oxygen with two negative charges (O''_i), and Ni^{3+} at Ni^{2+} regular lattice site with one positive charge ($Ni_{Ni}^{\bullet}$) i.e. oxidation of Ni^{2+} to Ni^{3+}. Nakamura et al. [22] reported suppression of O''_i formation with increase in acceptor content in K_2NiF_4-type materials. The partial substitution of Sr^{2+} for Sm^{3+}, thus, introduces extrinsic defects (Sr'_{Sm} and $Ni_{Ni}^{\bullet} = h^{\bullet}$) according to pseudo-reaction given below:

$$SrO + 3Ni_{Ni}^{x} + \frac{1}{2}O_2\downarrow \Leftrightarrow Sr'_{Sm} + 3Ni_{Ni}^{\bullet} + O''_i \quad (2)$$

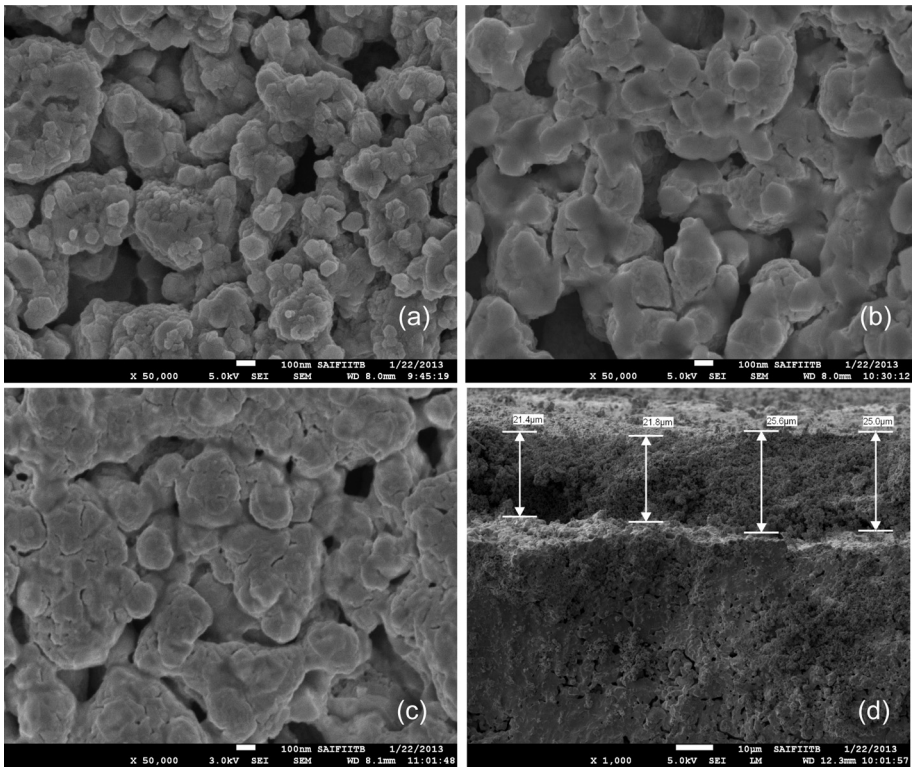

Fig. 3. Scanning electron microphotographs of cathode surface of (a) Cell-8, (b) Cell-9, (c) Cell-10, and (d) electrode–electrolyte interface of Cell-10.

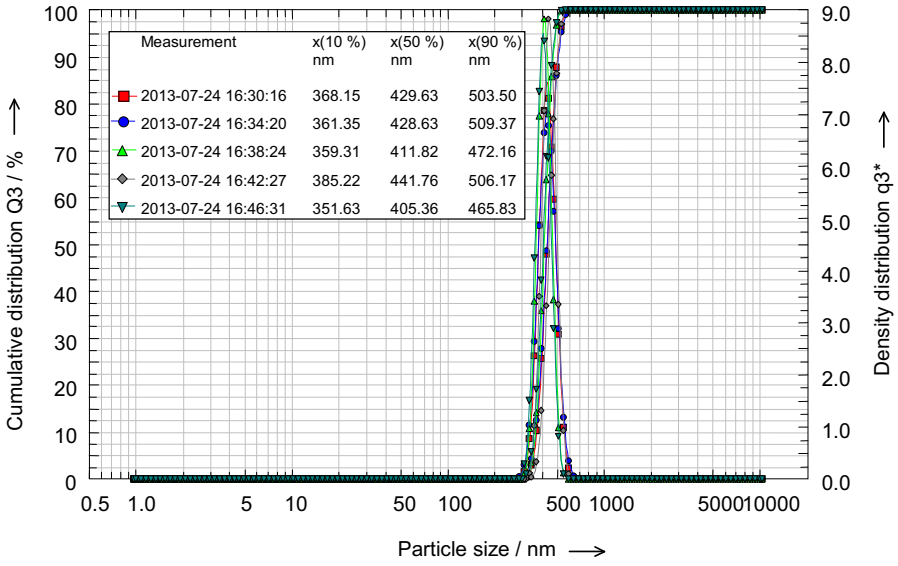

Fig. 4. Particle size distribution of $Sm_{1.5}Sr_{0.5}NiO_{4+\delta}$ in the prepared ink/slurry (five batches).

Concurrently, the electro-neutrality condition for $Sm_{2-x}Sr_xNiO_{4+\delta}$ with $\delta > 0$ is

$$2[O_i''] + [Sr'_{Sm}] = [Ni_{Ni}^{\bullet}] = [h^{\bullet}]. \quad (3)$$

Vashook et al. [13], also, proposed similar electro-neutrality condition for Sr substituted La_2NiO_4. The defects namely O_i'', Sr'_{Sm} and $Ni_{Ni}^{\bullet}/h^{\bullet}$ along with $V_O^{\bullet\bullet}$ remain dissociated for relatively lower Sr concentrations ($x \leq 0.5$) in $Sm_{2-x}Sr_xNiO_{4+\delta}$ lattice. Also, the suppression of O_i'' being negligible, interstitial oxygen concentration is sufficiently high for low Sr content. The initial increase (inset of Fig. 5) in electronic conductivity with increased acceptor content (Sr) is, thus, attributed to increased mobile charge carrier ($Ni_{Ni}^{\bullet}/h^{\bullet}$) density as per the defect chemistry (Eq. (2)). An enhancement in conductivity for low Sr content in $Pr_{2-x}Sr_xNiO_{4+\delta}$ is, also, reported in literature [23]. The associated extrinsic defects for relatively higher Sr concentrations ($x > 0.5$) leads to formation of electrically neutral clusters such as $V_O^{\bullet\bullet} + 2Sr'_{Sm} = (V_O^{\bullet\bullet}2Sr'_{Sm})^x$ and $Ni_{Ni}^{\bullet} + Sr'_{Sm} = (Ni_{Ni}^{\bullet}Sr'_{Sm})^x$. Petrov et al. [24], using theoretical and experimental data, explained the formation of electrically neutral defects associates or clusters. Both the clusters (which hinder the paths of mobile charge carriers) and the suppression of formation of O_i'' are responsible for decrease in dc conductivity for relatively higher acceptor Sr content. Vashook et al. [25] also explained Sr concentration dependent conductivity behavior of $La_{2-x}Sr_xNiO_4$ using similar concept of clusters. There is no conductivity data available related to present system in the literature for comparison. Since $Sm_{1.5}Sr_{0.5}NiO_{4+\delta}$ exhibited highest d.c. conductivity amongst all compositions under study, it was selected for further studies.

The variation of d.c. conductivity (σ) with oxygen partial pressure (P_{O_2}) for $Sm_{1.5}Sr_{0.5}NiO_{4+\delta}$, shown in Fig. 6, can be represented by equation given below:

$$\sigma = \sigma_0 (P_{O_2})^n \quad (4)$$

The absorption of oxygen gives rise to O_i'' and hole ($Ni_{Ni}^{\bullet}/h^{\bullet}$) in $Sm_{1.5}Sr_{0.5}NiO_{4+\delta}$ according to defect equilibrium given below:

$$\frac{1}{2}O_2(gas) \Leftrightarrow O_i'' + 2h^{\bullet} \quad (5)$$

The concentration of O_i'' and hole (h•), mobile charge carriers, thus, increases with increased P_{O_2} thereby enhancing d.c. conductivity (Fig. 6). Li et al. [26], also, reported increase in conductivity with P_{O_2}. The n values determined using Eq. (4) are 0.01 and 0.02 at 550 and 700 °C, respectively. Although, the values of n are lower than expected ($n = 0.25$), it indicates absorption of oxygen in oxide lattice. The small dependence of d.c. conductivity on P_{O_2} is in good agreement with the previous reporting [27].

3.4. Electrochemical impedance spectroscopy

The complex impedance plots at various temperatures for Cell-10 (as a representative) shown in Fig. 7 are distorted semicircular

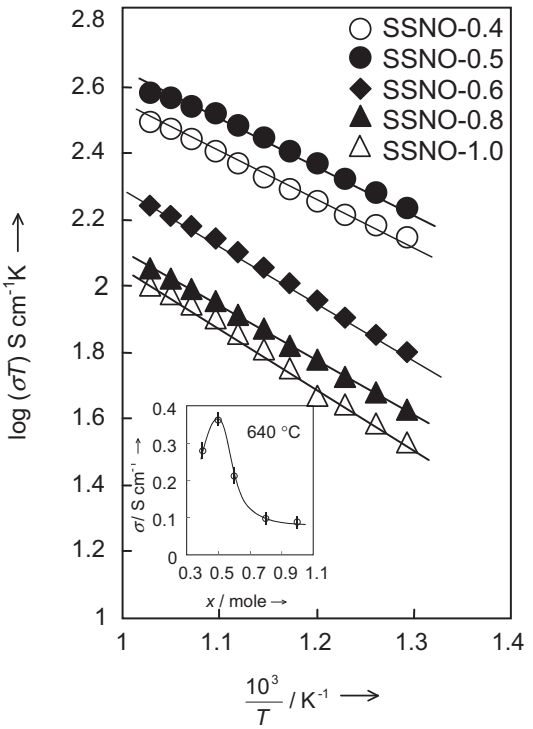

Fig. 5. Arrhenius plots for $Sm_{2-x}Sr_xNiO_{4+\delta}$ when $x = 0.4$–1.0; inset shows variation of σ with x at 640 °C.

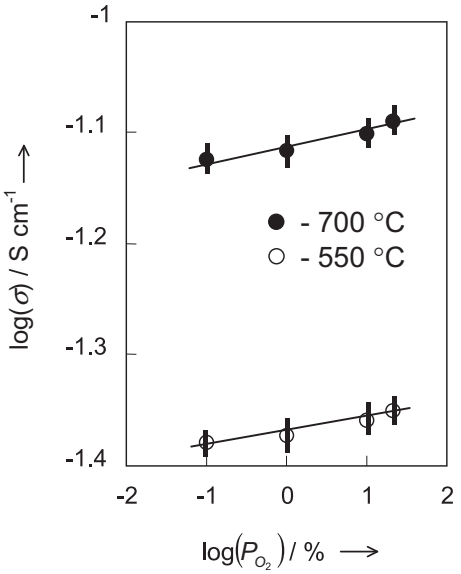

Fig. 6. Variation of σ with oxygen partial pressure at 700 and 550 °C for $Sm_{1.5}Sr_{0.5}NiO_{4+\delta}$.

arcs in the low frequency region. The absence of semicircular arc in the high frequency region is due to limitation of the available frequency (≤1 MHz). The high frequency intercept at real axis (R_{GDC}), however, is assigned to GDC electrolyte. The distorted semicircular arc in the low frequency region is attributed to the electrode. The real axis intercepts of semicircular arcs, as expected, are increased with decreasing temperature, which indicates increase in GDC electrolyte resistance (R_{GDC}) as well as ASR of the electrode. Similar responses were observed for Cell-8 and Cell-9 (not shown here). The experimental impedance spectrum, simulated response and electrical equivalent circuit model are shown in Fig. 7. As seen, the simulated curve (solid line obtained from the electrical equivalent model) fits well with the experimental data (symbols in Fig. 7). The low frequency response (Fig. 7) is, particularly, simulated with the Warburg impedance [28]. The values of simulated circuit elements at selected temperatures (640, 660, 680 and 700 °C) are presented in Table 3. As seen, both the R_{GDC} and the W–R (Warburg resistance) are increased with decrease in temperature in good agreement with the EIS plots (Fig. 7). Furthermore, the increase in corresponding W–T parameters with reduction in temperature suggests temperature-activated behavior.

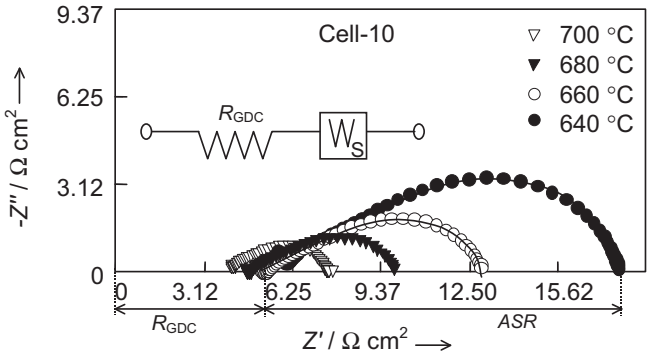

Fig. 7. Complex impedance plots for Cell-10 at various temperatures; experimental data (symbols/points), simulated data (solid line), and the electrical equivalent circuit model.

Table 3
The values of fitted circuit elements corresponding to electrochemical impedance spectra of Cell-10 at various temperatures.

Sr #.	T (°C)	R_{GDC} (ohm)	W–R (ohm)	W–$T \times (10^{-3})$	W–P
1	700	16.20 ± 1	13.75 ± 0.5	0.668 ± 0.07	0.363 ± 0.005
2	680	19.19 ± 1	21.14 ± 0.7	1.296 ± 0.09	0.376 ± 0.007
3	660	21.04 ± 2	31.70 ± 0.4	2.324 ± 0.06	0.375 ± 0.003
4	640	30.40 ± 1	68.80 ± 0.5	3.989 ± 0.08	0.329 ± 0.004

A temperature dependent ASR for Cell-8, Cell-9 and Cell-10 is shown in Fig. 8. Evidently, the Cell-10 exhibits lowest ASR (in the entire temperature range of measurements) amongst all the cells under study. The grains of $Sm_{1.5}Sr_{0.5}NiO_{4+\delta}$ remain agglomerated (Fig. 3(a) and (b)) in spite of sintering the symmetric cells at 800 and 900 °C for 2 h. Such agglomerated sub-micron sized grains result in relatively poor grain to grain contacts, which hinder the ionic as well as electronic mobility across the grains (inter-grain) resulting in high ASR for Cell-8 and Cell-9 (Fig. 8). Cell sintered at 1000 °C resulted in moderate grain growth giving rise to lesser agglomeration than those of Cell-8 and Cell-9. Reduced agglomeration leads to improved inter-grain contacts resulting in moderate porosity (Fig. 3(c)). Improved inter-grain contact lowers the ASR of Cell-10 compared to Cell-8 and Cell-9. The minimum value of ASR = 2.7 Ω cm^2 obtained at 700 °C is lower than the earlier reported ASR = 3.06 Ω cm^2 for $SmSrNiO_{4+\delta}$ [16]. Improved electrochemical performance is due to uniform particle size distribution with mean particle size 423 ± 11 nm of $Sm_{1.5}Sr_{0.5}NiO_{4+\delta}$ and optimal distribution of nano-pores in the cathode layer (Fig. 3(c)).

The complex impedance plots of Cell-10 at 700 °C for different oxygen partial pressures (P_{O_2}) are shown in Fig. 9(a). As seen, the x-axis intercept in the low-frequency domain (electrode) depends on P_{O_2}. The electrolytic resistance, however, remains invariant to P_{O_2} variations. The dependence of log (ASR) on log (P_{O_2}) at 700 °C is shown in Fig. 9(b). Evidently, the ASR of the electrode varies with P_{O_2} in accordance with the relation given below:

$$\mathrm{ASR} = (\mathrm{ASR})_0 (P_{O_2})^{-n} \quad (6)$$

The value of n provides useful information on the type of species involved in reactions that occur at the electrode [29].

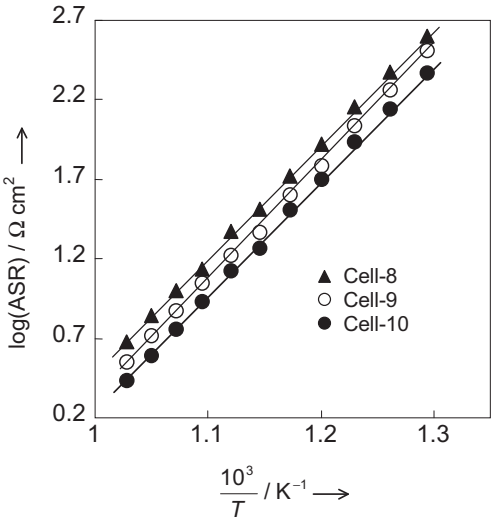

Fig. 8. Variation of area specific resistance (ASR) of symmetric cells when sintered at 800 (Cell-8), 900(Cell-9), and 1000 °C (Cell-10).

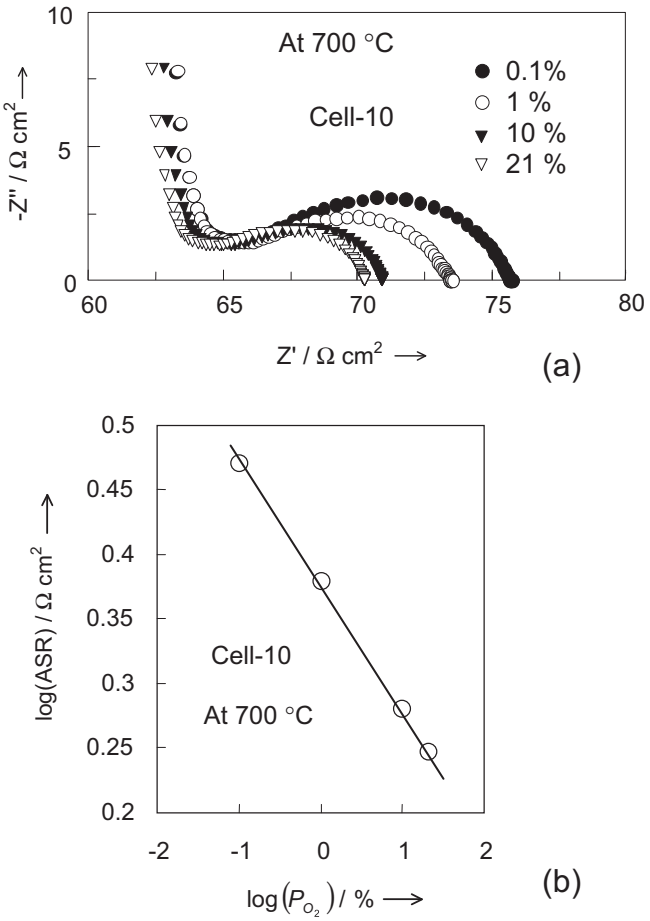

Fig. 9. (a) Complex impedance plots of Cell-10 at 700 °C for different oxygen partial pressures (b) variation of area specific resistance with oxygen partial pressure at 700 °C.

$$n = 1, \quad O_2(g) \Leftrightarrow O_{2(ads)} \tag{7}$$

$$n = \frac{1}{2}, \quad O_{2(ads)} \Leftrightarrow 2O_{(ads)} \tag{8}$$

$$n = \frac{1}{4}, \quad O_{(ads)} + 2e' + V_O^{\bullet\bullet} \Leftrightarrow O_O^x \tag{9}$$

$$n = \frac{1}{10}, \quad O_{TPB}^{2-} + V_O^{\bullet\bullet} \Leftrightarrow O_O^x \tag{10}$$

The $n = 0.2$ (estimated from Fig. 9(b) in the present study) indicates charge transfer is the rate-limiting step. Similarly, the $n \approx 0.25$ is reported due to the contribution of the charge transfer process on the Nd_2NiO_4 cathode [30]. According to literature, observed $n \approx 0.1$ (Eq. (10)) for LSM–YSZ cathode is attributed to oxygen ion transfer from the triple phase boundary (TPB) to the electrolyte [31]. A number of workers have analyzed the P_{O_2} dependent ASR behavior in MIECs, based on the Eqs. 7–10 [16,32–34].

It is well known that the interstitially substituted oxygen ions O_i'' of $Sm_{1.5}Sr_{0.5}NiO_{4+\delta}$ (excess oxygen ions) creates extrinsic holes ($h^\bullet$) so as to attain electrical neutrality according to Eq. (5). The O_i'' concentration is, thus, enhances with an increase in P_{O_2} that commensurately increased the mobile charge carrier ($h^\bullet$) density. The ASR, thus, reduces (Fig. 9(b)) with increase in P_{O_2}.

4. Conclusions

Solid solutions $Sm_{2-x}Sr_xNiO_{4+\delta}$ when $x = 0.4$–1.0 synthesized by combustion followed by sintering at 1100 °C for 10 h yield crystallite size in the range 73–82 nm. A single-phase $Sm_{2-x}Sr_xNiO_{4+\delta}$ solid solutions are of orthorhombic and tetragonal crystal structures when $x = 0.4$–0.7 and $x = 0.8$–1.0, respectively. The narrow particle size distribution with mean particle size 423 ± 11 nm of $Sm_{1.5}Sr_{0.5}NiO_{4+\delta}$ in its ink is obtained by ball milling at 300 rpm for 1 h. The maximum electronic conductivity ($\sigma = 0.361$ S cm^{-1} at 640 °C) in $Sm_{2-x}Sr_xNiO_{4+\delta}$ when $x = 0.5$ is attributed to the optimum mobile extrinsic defects ($h^\bullet$). The decrease in conductivity when $x > 0.5$ is understood to be due to the formation of electrical neutral clusters. The minimum area specific resistance (ASR) of 2.7 Ω cm^2 at 700 °C is obtained when $x = 0.5$, and is due to sub-micron sized grains and optimum porosity of the cathode. The $Sm_{1.5}Sr_{0.5}NiO_{4+\delta}$ solid solution with good electrocatalytic activity for oxygen reduction may be considered as a potential cathode material for IT-SOFC applications.

Acknowledgments

The authors are thankful to DST, New Delhi and EPSRC, Swindon, for financial support through Indo-UK multi-institutional project No. SR/RC-UK/Fuel-Cell-04/2011/RTM(G) to carry out this collaborative work. Mr. V.N. Chaudhari is thankful to UGC, New Delhi (India) for awarding UGC-BSR fellowship.

References

[1] P. Ganguly, C.N.R. Rao, Mat. Res. Bull. 8 (1973) 405–412.
[2] S.J. Skinner, J.A. Kilner, Solid State Ionics 135 (2000) 709–712.
[3] E. Boehm, J.M. Bassat, P. Dordor, F. Mauvy, J.C. Grenier, P. Stevens, Solid State Ionics 176 (2005) 2717–2725.
[4] J.M. Bassat, P. Odier, J.P. Loup, J. Solid State Chem. 110 (1994) 124–135.
[5] F. Mauvy, C. Lalanne, J.M. Bassat, J.C. Grenier, H. Zhao, P. Dordor, P. Stevens, J. Euro. Ceram. Soc. 25 (2005) 2669–2672.
[6] C. Lalanne, F. Mauvy, J.M. Bassat, J.C. Grenier, P. Stevens, G. Prosperi, J. Van Herle, F. Diethelm, R. Ihringer, 7th European SOFC Conference, Lucerne, Switzerland, 2006.
[7] C.N. Munnings, S.J. Skinner, G. Amow, P.S. Whitfield, I.J. Davidson, J. Fuel Cell Sci. Tech. 2 (2005) 34–37.
[8] D. Pérez-Coll, A. Aguadero, M.J. Escudero, P. Núñez, L. Daza, J. Power Sources 178 (2008) 151–162.
[9] J. Jorgensen, B. Dabrowski, S. Pei, D. Richards, D. Hinks, Phys. Rev. B 40 (1989) 2187–2199.
[10] A. Mehta, P.J. Heaney, Phys. Rev. B 49 (1994) 401–571.
[11] M.A. Daroukh, V.V. Vashook, H. Ullmann, F. Tietz, I. Arual Raj, Solid State Ionics 158 (2003) 141–150.
[12] V.V. Vashook, N.E. Trofimenko, H. Ullmann, L.V. Makhnach, Solid State Ionics 131 (2000) 329–336.
[13] V.V. Vashook, I.I. Yushkeivich, L.V. Kokhonovsky, L.V. Makhonovsky, L.V. Makhanch, S.P. Tolochko, I.F. Kononyuk, H. Ullmann, H. Altenburg, Solid State Ionics 119 (1999) 23–30.
[14] V.V. Vashook, S.P. Tolochko, I.I. Yushkeivich, L.V. Makhanch, I.F. Kononyuk, H. Altenburg, J. Hauck, H. Ullmann, Solid State Ionics 110 (1998) 245–253.
[15] K. Ishikawa, S. Kondo, H. Okanc, S. Suzuki, Y. Suzuki, Bull. Chem. Soc. Jpn. 60 (2006) 1174–1178.
[16] Q. Li, Y. Fan, H. Zhao, L.P. Sun, L.H. Huo, J. Power Sources 167 (2007) 64–68.
[17] A.P. Khandale, S.S. Bhoga, J. Power Sources 195 (2010) 7974–7982.
[18] A.P. Khandale, S.S. Bhoga, J. Solid State Electrochem. 16 (2012) 341–352.
[19] H. Lou, Y. Ge, P. Chen, M. Mei, F. Ma, G. Lu, J. Mater. Chem. 7 (1997) 2097–2101.
[20] P. Ganguly, C.N.R. Rao, J. Solid State Chem. 53 (1984) 193–216.
[21] R.D. Shannon, Acta Crystallogr. Sect. A 32 (1976) 751–767.
[22] T. Nakamura, K. Yashiro, K. Sato, J. Mizusaki, Solid State Ionics 181 (2010) 292–299.
[23] J. Yang, J. Cheng, Q. Jiang, Y. Wang, R. Wang, J. Gao, Int. J. Hydrogen Energy 37 (2012) 1746–1751.
[24] A.N. Petrov, A.Y. Zuev, M.A. Degtyarev, J. Inorg. Chem. Rus. 72 (1998) 44–49.
[25] V.V. Vashook, E. Girdauskaite, J. Zosel, T.L. Wen, H. Ullman, U. Guth, Solid State Ionics 177 (2006) 1163–1171.
[26] Z. Li, R. Haugsrud, J.B. Smith, T. Norby, Solid State Ionics 180 (2009) 1433–1441.

[27] V.I. Voronin, A.E. Kar'kin, B.N. Goshchitski, A. Yu Zuev, T.P. Rodionova, A.N. Petrov, Phys. Solid State 40 (1998) 157–162.
[28] D.R. Franceschetti, J.R. Macdonald, J. Electrochem. Soc. 138 (1991) 1368–1371.
[29] E. Siebert, A. Hammouche, M. Cleitz, Electrochim. Acta 40 (1995) 1741–1753.
[30] F. Mauvy, C. Lalanne, J.M. Bassat, J.C. Grenier, H. Zhao, L. Huo, P. Stevens, J. Electrochem. Soc. 153 (2006) A1547–A1553.
[31] J.D. Kim, G.D. Kim, J.W. Moon, Y.I. Park, W.H. Lee, K. Kobayashi, M. Nagai, C.F. Kim, Solid State Ionics 143 (2001) 379–389.
[32] A. Aguadero, J.A. Alonso, M.J. Escudero, L. Daza, Solid State Ionics 179 (2008) 393–400.
[33] L.P. Sun, Q. Li, H. Zhao, L.H. Huo, J.C. Grenier, J. Power Sources 183 (2008) 43–48.
[34] Q. .Li, Y. .Fan, H. Zhao, L.H. Huo, J. Chin., Inorg. Chem. 22 (2006) 2025–2030.